Application of the method of equivalent edge currents to composite scattering from the cone-cylinder above a dielectric rough sea surface*

Guo Li-Xin(郭立新)†, Wang Rui(王 蕊), and Wu Zhen-Sen(吴振森)

School of Science, Xidian University, Xi'an 710071, *China*

(Received 12 August 2009; revised manuscript received 27 August 2009)

Compared with scattering from a rough surface only, composite scattering from a target above a rough surface has become so practical that it is a subject of great interest. At present, this problem has been solved by some numerical methods which will produce an enormous calculation amount. In order to overcome this shortcoming, the reciprocity theorem (RT) and the method of equivalent edge currents (MEC) are used in this paper. Due to the advantage of RT, the difficulty in computing the secondary scattered fields is reduced. Simultaneously, MEC, a high-frequency method with edge diffraction considered, is used to calculate the scattered field from the cone-cylinder target with a high accuracy and efficiency. The backscattered field and the polarization currents of the rough sea surface are evaluated by the Kirchhoff approximation (KA) method and physical optics (PO) method, respectively. The effects of the backscattering radar cross section (RCS) and the Doppler spectrum on the size of the target and the windspeed of the sea surface for different incident angles are analysed in detail.

Keywords: method of equivalent edge currents, reciprocity theorem, cone-cylinder, rough sea surface, electromagnetic scattering

PACC: 4120, 4110H

1. Introduction

In recent years, composite electromagnetic scattering between a randomly rough surface and a target has attracted considerable interest in the fields of radar surveillance, target tracking and oceanic remote sensing, etc. The electromagnetic scattering from a target above a rough surface has received more and more attention from many researchers[1−7] and some numerical approaches[8−12] such as the method of moments (MOM), finite-difference time-domain method (FDTD), forward–backward method (FBM), generalized FBM (GFBM), FBM spectrum accelerate algorithm (FBM/SAA), finite element method (FEM) and iterative method have been applied to the electromagnetic scattering from a one-dimensional (1D) model of an object and the oceanic surface. However, the elements of the impedance matrix and the surface electric and magnetic currents of the lossy dielectric ocean must be determined and evaluated again at different moments due to the variation of the ocean with time, and the numerical algorithm will produce an enormous calculation amount, especially for a large scale rough surface with low grazing angle incidence. In addition, there are few numerical methods applied to the problem of scattering from the two-dimensional (2D) case[13,14] at present due to the fact that unknowns of the large 2D surface in the algorithm become extremely large. Hence, this subject still needs further investigation. Another point that is worth noting is that in previous work, edge diffraction of the target was often neglected in the composite scattering model. To solve the above mentioned problem, the reciprocity theorem (RT) and the method of equivalent edge currents (MEC) are introduced in this paper, the currents and the backscattering field of the sea surface are derived by using the physical optics (PO) and Kirchhoff approximation (KA) methods, respectively. The backscattered field from the cone-cylinder is used by the MEC method with consideration of the edge diffraction, and then, based on the RT,[1] the secondary scattered fields between the cone-cylinder and the sea surface is reduced. This paper provides a method for studying the composite scattering from an electrical large-size target and a rough surface.

*Project supported by the National Natural Science Foundation of China (Grant No. 60971067) and the Specialized Research Fund for the Doctoral Program of Higher Education of China (Grant No. 20070701010).

†Corresponding author. E-mail: lxguo@mail.xidian.edu.cn

© 2010 Chinese Physical Society and IOP Publishing Ltd

The rest of the present paper is organized as follows. Formulae for the currents and the backscattering field of the rough sea surface are derived by using the PO and KA methods in Section 2. The scattering from the cone-cylinder is briefly presented by the MEC method in Section 3. The composite scattering field is solved based on the RT in Section 4. The numerical results of the composite backscattering are presented and discussed in Section 5. Section 6 ends with the conclusions of the paper and a proposition for further investigation in this topic.

2. Scattered field from a rough sea surface

For the scattering computation, surface realizations are needed at a set of P points with spacing Δx over a length of $L = P\Delta x$. Realizations with the desired properties can be generated at points $x_p = p\Delta x$ $(p = 1, \ldots, p)$ using[15]

$$f(x_p, t) = \frac{1}{L} \sum_{m=-P/2+1}^{P/2} \tilde{\varsigma}(K_\mathrm{m}, t) \exp(-\mathrm{i} K_\mathrm{m} x_p), \tag{1}$$

where for $m \geq 0$,

$$\tilde{\varsigma}(K_\mathrm{m}) = \sqrt{2\pi L W(K_\mathrm{m})} \exp(\mathrm{i}\omega(K_\mathrm{m})t) \begin{cases} [N(0,1) + \mathrm{i}N(0,1)]/\sqrt{2}, & m \neq 0, P/2, \\ N(0,1), & m = 0, P/2 \end{cases} \tag{2}$$

with $\omega(K_\mathrm{i}) = \{g_0 |K_\mathrm{i}| [1 + (K_\mathrm{i}/363.2)^2]\}^{1/2}$; for $m < 0$, $\tilde{\varsigma}(K_\mathrm{m}) = \tilde{\varsigma}^*(K_{-\mathrm{m}})$ with $K_\mathrm{m} = 2\pi m/L$ and the symbol $*$ representing the complex conjugation. $N(0,1)$ appears each time, which indicates an independent sample taken from a zero mean, unit variance Gaussian distribution. For the present work, the rough surface used in the scattering model is generated randomly with a Pierson–Moskowitz (PM) spectrum,[15] i.e.

$$W(K_\mathrm{m}) = \frac{\alpha}{4K_\mathrm{m}^3} \exp\left(-\frac{\beta g_0^2}{K_\mathrm{m}^2 U_{19.5}^4}\right), \tag{3}$$

where K_m refers to the spatial wave-number, $g_0 = 9.81\ \mathrm{m/s^2}$ is the gravity acceleration, $U_{19.5}$ represents the windspeed at a height of 19.5 m above the mean surface $z = 0$, and constants $\alpha = 8.1 \times 10^{-3}$ and $\beta = 0.74$. The rough sea surface can be simulated from Eq. (1) by the fast Fourier transform (FFT).

Consider an electromagnetic (EM) wave with a unit amplitude that irradiates the rough sea surface extending from $-L$ to L. Using the KA theory, the scattered field from the ocean can be written as[16]

$$E^\mathrm{s}(r) = \frac{\mathrm{i}k \exp(\mathrm{i}kr)}{4\pi\ r} \int_{-L}^{L} (p f'_x(x,t) - q) \times \exp \mathrm{i}[v_x x + v_z f(x,t)] \mathrm{d}x, \tag{4}$$

where

$$p = (1 - R)\sin\theta_\mathrm{i} + (1 + R)\sin\theta_\mathrm{s}, \tag{5}$$

$$q = (1 + R)\cos\theta_\mathrm{s} - (1 - R)\cos\theta_\mathrm{i}, \tag{6}$$

$$v_x = k(\sin\theta_\mathrm{i} - \sin\theta_\mathrm{s}), \tag{7}$$

$$v_z = -k(\cos\theta_\mathrm{i} + \cos\theta_\mathrm{s}) \tag{8}$$

with θ_i and θ_s being the incident angle and the scattering angle, respectively. In the backscattering direction, $\theta_\mathrm{s} = -\theta_\mathrm{i}$. The parameter R denotes the Fresnel reflection coefficient of the tangential plane at the point of interest, which is given by

$$R_\mathrm{vv} = \frac{\varepsilon_\mathrm{r}\cos\theta_\mathrm{l} - (\varepsilon_\mathrm{r} - \sin^2\theta_\mathrm{l})^{1/2}}{\varepsilon_\mathrm{r}\cos\theta_\mathrm{l} + (\varepsilon_\mathrm{r} - \sin^2\theta_\mathrm{l})^{1/2}},$$

and

$$R_\mathrm{hh} = \frac{\cos\theta_\mathrm{l} - (\varepsilon_\mathrm{r} - \sin^2\theta_\mathrm{l})^{1/2}}{\cos\theta_\mathrm{l} + (\varepsilon_\mathrm{r} - \sin^2\theta_\mathrm{l})^{1/2}}, \tag{9}$$

where θ_l is the local incident angle (the angle between the incident wave direction and the oceanic surface normal at the point x) and ε_r is the relative dielectric constant of the surface. If the average slope of the oceanic surface is small, the local incident angle can be replaced by the incident angle θ_i.

Let a plane wave $\boldsymbol{E}_\mathrm{i} = \hat{\boldsymbol{y}} \exp(\mathrm{i}\boldsymbol{k} \cdot \boldsymbol{r})$ (hh-polarization) irradiate the dynamic ocean. If the condition of validity of the standard KA is satisfied in modelling the EM scattering from the ocean, the surface electric and magnetic currents can be calculated by PO, which yields[17]

$$\boldsymbol{J}_{\rm rte} = (1 - R_{\rm hh})\hat{\boldsymbol{n}} \times \boldsymbol{H}_{\rm i} = (1 - R_{\rm hh})\sqrt{\frac{\varepsilon}{\mu}}\frac{(\cos\theta_{\rm i} + f'_x \sin\theta_{\rm i})}{\sqrt{1 + f'^2_x}} \exp({\rm i}kx\sin\theta_{\rm i} - {\rm i}kf\cos\theta_{\rm i})\hat{\boldsymbol{y}}, \tag{10}$$

$$\boldsymbol{M}_{\rm rte} = -(1 + R_{\rm hh})\hat{\boldsymbol{n}} \times \boldsymbol{E}_{\rm i} = (1 + R_{\rm hh})\frac{\hat{\boldsymbol{x}} + f'_x\hat{\boldsymbol{z}}}{\sqrt{1 + f'^2_x}} \exp({\rm i}kx\sin\theta_{\rm i} - {\rm i}kf\cos\theta_{\rm i}). \tag{11}$$

On the other hand, the scattered field can also be given by the well-known Stratton–Chu formula,[17] i.e.

$$\boldsymbol{E}^{\rm s}_{\rm r}(\boldsymbol{r}, \boldsymbol{r}') = {\rm i}\omega\mu \iint_{s'} \left[\bar{\bar{\boldsymbol{G}}}\,(\boldsymbol{r}, \boldsymbol{r}') \cdot \frac{\exp({\rm i}k|\boldsymbol{r} - \boldsymbol{r}'|)}{4\pi|\boldsymbol{r} - \boldsymbol{r}'|}\boldsymbol{J}_{\rm rte} + \boldsymbol{\nabla}\times \bar{\bar{\boldsymbol{G}}}\,(\boldsymbol{r}, \boldsymbol{r}') \cdot \boldsymbol{M}_{\rm rte}\right] {\rm d}s', \tag{12}$$

where the dyadic Green function $\bar{\bar{\boldsymbol{G}}} = (\bar{\bar{\boldsymbol{I}}} + \nabla\nabla/k^2)$. Substituting Eqs. (10) and (11) into Eq. (12), the expression for the scattered field, which is completely coincident with Eq. (4), is obtained in the far-field zone. Similarly, when the surface is irradiated by the incident field $\boldsymbol{H}_{\rm i} = \hat{\boldsymbol{y}}\sqrt{\varepsilon/\mu}\exp({\rm i}\boldsymbol{k}\cdot\boldsymbol{r})$ (vv-polarization), the electric and the magnetic currents on the surface can be written as

$$\boldsymbol{J}_{\rm rtm} = (1 + R_{\rm vv})\hat{\boldsymbol{n}} \times \boldsymbol{H}_{\rm i} = -(1 + R_{\rm vv})\frac{\hat{\boldsymbol{x}} + f'_x\hat{\boldsymbol{z}}}{\sqrt{1 + f'^2_x}} \exp({\rm i}k\sin\theta_{\rm i} - {\rm i}kf\cos\theta_{\rm i}), \tag{13}$$

$$\boldsymbol{M}_{\rm rtm} = -(1 - R_{\rm vv})\hat{\boldsymbol{n}} \times \boldsymbol{E}_{\rm i} = (1 - R_{\rm vv})\frac{\cos\theta_{\rm i} + f'\sin\theta_{\rm i}}{\sqrt{1 + f'^2_x}} \exp({\rm i}kx\sin\theta_{\rm i} - {\rm i}kf\cos\theta_{\rm i})\hat{\boldsymbol{y}}. \tag{14}$$

3. Scattered field from the cone-cylinder with MEC

As far as MEC is concerned, the explicit GTD-MEC expressions for an arbitrary local wedge angle and arbitrary direction for irradiation and observation were derived by Michaeli.[18] MEC is applicable to the theory with consideration of the electromagnetic high frequency diffraction by edges. However, there are many singularities in the implementation of this method. To eliminate the singularities, some new expressions were derived for the fringe current components of the equivalent edge currents, which are finite for all directions of irradiation and observation, except for the special case where the direction of observation is the continuation of a glancing incident ray propagating "inwards" with respect to the wedge surface.[19] According to the research by Ando *et al.*,[20−23] Cui *et al.*[24] derived the quasi-uniformity expressions of PO-MEC just including a real singularity by choosing the integral direction with the incremental-diffraction theory, which is called the comprehensive analysis of the total field method. In the present paper, the scattered field from a cone-cylinder is calculated by combining the comprehensive analysis with the PTD-MEC of Machaeli.

The basic idea of the MEC method is to assume the equivalent electric and magnetic currents I and M to be existent on the discontinuity edge C, and the diffracted field to be acquirable for the Fresnel and far zones by the radiation integral[18]

$$\boldsymbol{E}_{\rm s} = {\rm i}k\int_C [Z_0 I(\boldsymbol{r}')\hat{\boldsymbol{s}} \times (\hat{\boldsymbol{s}} \times \hat{\boldsymbol{t}}) + M(\boldsymbol{r}')(\hat{\boldsymbol{s}} \times \hat{\boldsymbol{t}})] \times \frac{\exp(-{\rm i}ks)}{4\pi s}{\rm d}l, \tag{15}$$

where $k = 2\pi/\lambda$ is the wavenumber of the incident wave; $Z_0 = \sqrt{\mu/\varepsilon}$ is the characteristic impedance of the medium, $\hat{\boldsymbol{s}} = \boldsymbol{s}/s = (\boldsymbol{r} - \boldsymbol{r}')/|\boldsymbol{r} - \boldsymbol{r}'|$ is the direction of observation of the radiating edge element at $\boldsymbol{r}'$ on C. In Fig. 1, $s = |\boldsymbol{r}' - \boldsymbol{r}|$, $\boldsymbol{r}$ is the vector of the observation point P. Figure 2 shows the wedge scattering geometry, where $\hat{\boldsymbol{s}}'$ is the direction of the incident wave, $\hat{\boldsymbol{t}}$ is the tangent unit vector, β' is the separation angle between $-\hat{\boldsymbol{t}}$ and the direction of the incident wave, β is the separation angle between $\hat{\boldsymbol{s}}$ and $\hat{\boldsymbol{t}}$, φ is the separation angle between $\hat{\boldsymbol{x}}$ and the projection of $\hat{\boldsymbol{s}}$ in the xy-plane, and φ' is the separation angle between $\hat{\boldsymbol{x}}$ and the projection of $\hat{\boldsymbol{s}}'$ in the xy-plane. $I(\boldsymbol{r}') = I^{\rm PO} + I^{\rm PTD}$ and $M(\boldsymbol{r}') = M^{\rm PO} + M^{\rm PTD}$ can each be split into PO and PTD components.

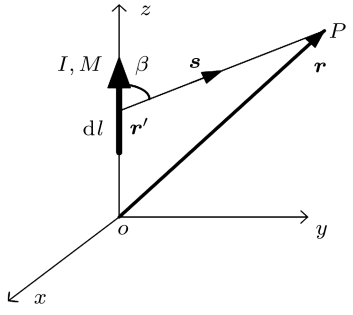


Fig. 1. Radiation field of the equivalent currents.

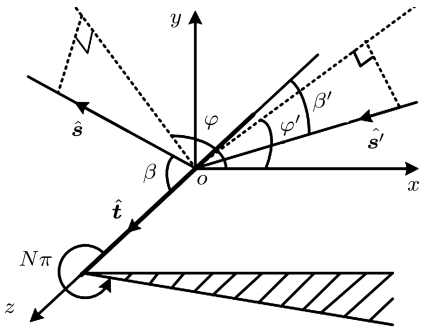


Fig. 2. Wedge scattering geometry.

The expressions for $I(\boldsymbol{r}')$ and $M(\boldsymbol{r}')$ from the comprehensive analysis method are as follows:[25]

$$I^{\mathrm{PO}} = \frac{2\mathrm{i}\boldsymbol{E}_0^i\cdot\hat{\boldsymbol{t}}}{k_0\eta_0\sin^2\beta'}D_{\mathrm{e}}^{\mathrm{PO}} + \frac{2\mathrm{i}\boldsymbol{H}_0^i\cdot\hat{\boldsymbol{t}}}{k_0\sin\beta'}D_{\mathrm{em}}^{\mathrm{PO}}, \quad (16)$$

$$M^{\mathrm{PO}} = \frac{2\mathrm{i}Z_0\boldsymbol{H}_0^i\cdot\hat{\boldsymbol{t}}}{k\sin\beta'\sin\beta}D_{\mathrm{m}}^{\mathrm{PO}}, \quad (17)$$

$$D_{\mathrm{e}}^{\mathrm{PO}} = \frac{\sin\varphi'\sin\beta' X_1}{X_1^2+Y_1^2}U_1 + \frac{\sin\pi-\varphi'\sin\beta' X_2}{X_2^2+Y_2^2}U_2, \quad (18)$$

$$D_{\mathrm{m}}^{\mathrm{PO}} = -\left\{\frac{\sin\varphi\sin\beta' X_1}{X_1^2+Y_1^2}U_1 + \frac{\sin\pi-\varphi\sin\beta' X_2}{X_2^2+Y_2^2}U_2\right\}, \quad (19)$$

$$D_{\mathrm{em}}^{\mathrm{PO}} = \frac{(\cos\beta\cos\varphi\sin\beta'+\cos\beta'\cos\varphi'\sin\beta)X_1}{(X_1^2+Y_1^2)\sin\beta}U_1 + \frac{(\cos\beta\cos(N\pi-\varphi)\sin\beta'+\cos\beta'\cos\pi-\varphi'\sin\beta)X_2}{(X_2^2+Y_2^2)\sin\beta}U_2, \quad (20)$$

$$\begin{aligned} X_1 &= \sin\beta\cos\varphi+\sin\beta'\cos\varphi',\\ X_2 &= \cos\pi-\varphi\sin\beta+\cos(N\pi-\varphi')\sin\beta',\\ Y_1 &= \cos\beta-\cos\beta',\\ Y_2 &= Y_1, \end{aligned} \quad (21)$$

$$\begin{aligned} U_1 &= U(\pi-\varphi'),\\ U_2 &= U[(1-N)\pi+\varphi')],\\ U(x) &= \begin{cases} 1 & x\geq 0\\ 0 & x<0 \end{cases}. \end{aligned} \quad (22)$$

The expressions for I^{PTD} and M^{PTD} come from the PTD–MEC method which was firstly proposed by Michaeli[19] for calculating the diffracted field.

The scattering geometries of the cylinder and the cone-cylinder are depicted in Fig. 3, where the geometrical parameters $a = 5$ cm and $h = 15$ cm are taken as an example, and the results of bistatic scattering from the above target with the MEC method are presented in Fig. 4 and Fig. 5 respectively, where the incident wave propagates along the direction of $\theta_{\mathrm{i}} = 0^\circ$, and $\varphi_{\mathrm{i}} = 0^\circ$ and the electric field polarizes along the direction of $\hat{\theta}$, the frequency of the incident wave is 10 GHz. From the scattering patterns, it is readily found that the results of the MEC method in this paper show good consistency with those of the MOM, which indicates the validity of the MEC method in this paper. Moreover, the MEC method has a higher efficiency than the MOM since it is a high frequency method and this method can be applied to the calculation of the EM scattering from electrical large-size targets with consideration of the edge currents and the edge diffraction.

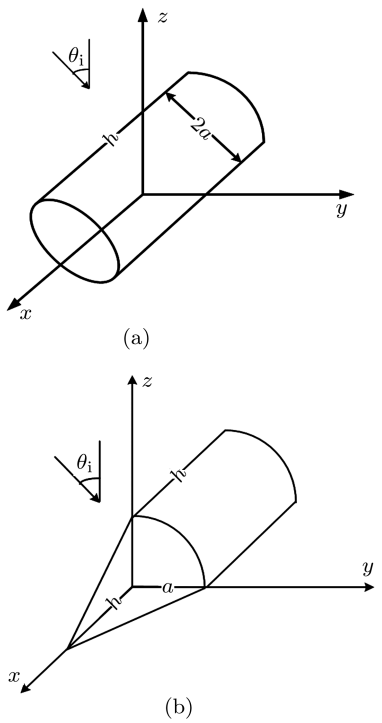


Fig. 3. Scattering geometry of the cylinder and the cone-cylinder.

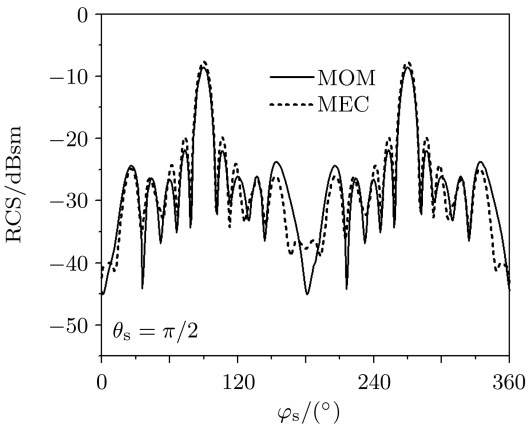


Fig. 4. Bistatic RCS of the cylinder.

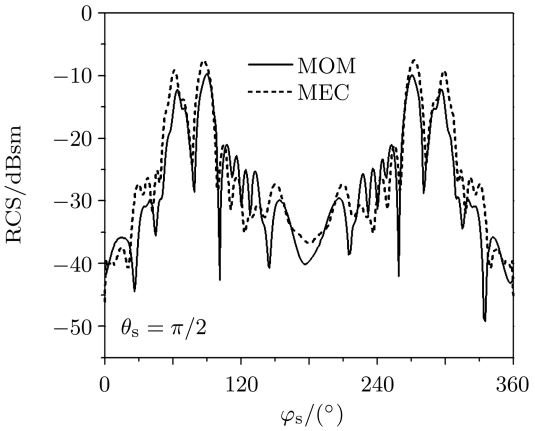


Fig. 5. Bistatic RCS of the cone-cylinder.

4. Coupling scattered field between the cone-cylinder and the rough sea surface

In this Section, the RT is used to calculate the coupling field between the cone-cylinder and the rough sea surface. Figure 6 shows the geometry of composite scattering between the cone-cylinder and the sea surface. For the case of hh-polarization (TE case), assume the elementary electric and magnetic currents $\boldsymbol{J}_e = \hat{y}\delta(\boldsymbol{r} - \boldsymbol{r}_0)$ and $\boldsymbol{M}_e = -\hat{\theta}\delta(\boldsymbol{r} - \boldsymbol{r}_0)$ to be existent in the far zone r_0 and the EM fields produced by them can be denoted as[1]

$$\boldsymbol{E}_{ed}(\boldsymbol{r}) = E_0 \exp(\mathrm{i}\boldsymbol{k}_i \cdot \boldsymbol{r})\hat{y}, \tag{23}$$

$$\boldsymbol{H}_{md}(\boldsymbol{r}) = -H_0 \exp(\mathrm{i}\boldsymbol{k}_i \cdot \boldsymbol{r})\hat{\theta}, \tag{24}$$

where $E_0 = \mathrm{i}kZ_0/(4\pi r_0)\exp(\mathrm{i}kr_0)$, $H_0 = \mathrm{i}kY_0/(4\pi r_0)\exp(\mathrm{i}kr_0)$, and Y_0 is the characteristic admittance of the medium. Consider the cone-cylinder irradiated by a plane wave $\boldsymbol{E}_h^i = \exp(\mathrm{i}\boldsymbol{k}_s \cdot \boldsymbol{r})\hat{y}$ and the corresponding scattered field may be expressed as $\boldsymbol{E}_h^s = \hat{\theta}E_{h\theta}^s + \hat{\varphi}E_{h\varphi}^s$ by using Eq. (15). Thereby the scattered field of the cone-cylinder illuminated by $\boldsymbol{E}_{ed}$ can be expressed as $\boldsymbol{E}_{hec}^s = E_0(\hat{\theta}E_{h\theta}^s + \hat{\varphi}E_{h\varphi}^s)$. By using the RT, the coupling scattered fields of the composite model (shown as in Fig. 6) are obtained as

$$\begin{aligned}
\hat{\boldsymbol{y}} \cdot \boldsymbol{E}_{h,rc}^s &= \int_S \boldsymbol{J}_{rte} \cdot \boldsymbol{E}_{hec}^s \,\mathrm{d}S \\
&= \int_S (1 - R_{hh})\sqrt{\frac{\varepsilon}{\mu}} \frac{(\cos\theta_i + f_x' \sin\theta_i)}{\sqrt{1 + f_x'^2}} \exp(\mathrm{i}kx\sin\theta_i - \mathrm{i}kf\cos\theta_i)\hat{\boldsymbol{y}} \cdot \boldsymbol{E}_{hec}^s \,\mathrm{d}S \\
&= (1 - R_{hh})E_0\sqrt{\frac{\varepsilon}{\mu}} \int_S \frac{(\cos\theta_i + f_x' \sin\theta_i)}{\sqrt{1 + f_x'^2}} \exp(\mathrm{i}kx\sin\theta_i - \mathrm{i}kf\cos\theta_i) \\
&\quad \times (\cos\theta\sin\varphi E_{h\theta}^s + \cos\varphi E_{h\varphi}^s)\,\mathrm{d}S,
\end{aligned} \tag{25}$$

$$\begin{aligned}
-\hat{\theta} \cdot \boldsymbol{H}_{h,rc}^s &= \int_S \boldsymbol{M}_{rte} \cdot \boldsymbol{H}_{hmc}^s \,\mathrm{d}S \\
&= (1 + R_{hh}) \int_S \frac{1}{\sqrt{1 + f_x'^2}} \exp(\mathrm{i}kx\sin\theta_i - \mathrm{i}kf\cos\theta_i)(\hat{x} + f_x'\hat{z}) \cdot \boldsymbol{H}_{hmc}^s \,\mathrm{d}S \\
&= (1 + R_{hh})H_0 \int_S \frac{1}{\sqrt{1 + f_x'^2}} \exp(\mathrm{i}kx\sin\theta_i - \mathrm{i}kf\cos\theta_i) \\
&\quad \times [f_x' \sin\theta E_{h\varphi}^s - (\cos\theta\cos\varphi E_{h\varphi}^s + \sin\varphi E_{h\theta}^s)]\,\mathrm{d}S.
\end{aligned} \tag{26}$$

Here, $\boldsymbol{H}_{hmc}^s = H_0(-\hat{\theta}E_{h\varphi}^s + \hat{\varphi}E_{h\theta}^s)$ is the scattered field from the cone-cylinder irradiated by $\boldsymbol{H}_{md}$. Then, from Eqs. (25) and (26), the coupling scattered fields $\boldsymbol{E}_{h,rc_total}^s$ for the hh-polarization may be written as

$$\boldsymbol{E}_{h,rc_total}^s = \hat{y}(E_{h,rc}^s - Z_0 H_{h,rc}^s). \tag{27}$$

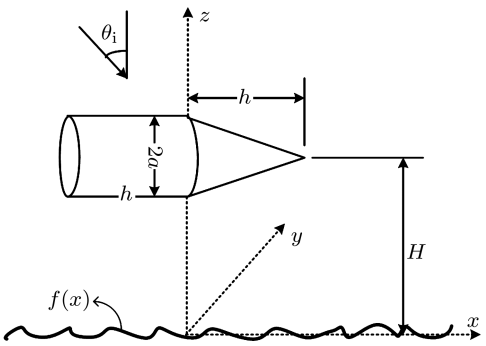


Fig. 6. Geometry of composite scattering between the cone-cylinder and the sea surface.

For the case of vv-polarization (TM case), assume the elementary electric and magnetic currents $\boldsymbol{J}_{\rm e} = \hat{\theta}\delta(\boldsymbol{r}-\boldsymbol{r}_0)$ and $\boldsymbol{M}_{\rm e} = \hat{y}\delta(\boldsymbol{r}-\boldsymbol{r}_0)$ to be existent in the far zone r_0 and their produced EM fields to be denotable as

$$\boldsymbol{E}_{\rm ed}(\boldsymbol{r}) = E_0 \exp(\mathrm{i}\boldsymbol{k}_{\rm i}\cdot\boldsymbol{r})\hat{\theta}, \tag{28}$$

$$\boldsymbol{H}_{\rm md}(\boldsymbol{r}) = H_0 \exp(\mathrm{i}\boldsymbol{k}_{\rm i}\cdot\boldsymbol{r})\hat{y}. \tag{29}$$

Similarly, using RT, the coupling scattered fields can be obtained as

$$\begin{aligned}
\hat{\boldsymbol{\theta}}\cdot\boldsymbol{E}^{\rm s}_{\rm v,rc} &= \int_S \boldsymbol{J}_{\rm rtm}\cdot\boldsymbol{E}^{\rm s}_{\rm vec}\,\mathrm{d}S \\
&= -(1+R_{\rm vv})\sqrt{\frac{\varepsilon}{\mu}}\int_S \frac{1}{\sqrt{1+f_x'^2}}\exp(\mathrm{i}kx\sin\theta_{\rm i}-\mathrm{i}kf\cos\theta_{\rm i})(\hat{x}+f_x'\hat{z})\cdot\boldsymbol{E}^{\rm s}_{\rm vec}\,\mathrm{d}S \\
&= -(1+R_{\rm vv})E_0\sqrt{\frac{\varepsilon}{\mu}}\int_S \frac{1}{\sqrt{1+f_x'^2}}\exp(\mathrm{i}kx\sin\theta_{\rm i}-\mathrm{i}kf\cos\theta_{\rm i}) \\
&\quad\times[(\cos\theta\cos\varphi E^{\rm s}_{\rm v\theta}-\sin\varphi E^{\rm s}_{\rm v\varphi})-f_x'\sin\theta E^{\rm s}_{\rm v\theta}]\,\mathrm{d}S, \qquad (30)\\
\hat{\boldsymbol{y}}\cdot\boldsymbol{H}^{\rm s}_{\rm v,rc} &= \int_S \boldsymbol{M}_{\rm rtm}\cdot\boldsymbol{H}^{\rm s}_{\rm vmc}\,\mathrm{d}S \\
&= (1-R_{\rm vv})\int_S \frac{\cos\theta_{\rm i}+f_x'\sin\theta_{\rm i}}{\sqrt{1+f_x'^2}}\exp(\mathrm{i}ky\sin\theta_{\rm i}-\mathrm{i}kf\cos\theta_{\rm i})\hat{y}\cdot\boldsymbol{H}^{\rm s}_{\rm vm2c}\,\mathrm{d}S \\
&= (1-R_{\rm vv})H_0\int_S \frac{\cos\theta_{\rm i}+f_x'\sin\theta_{\rm i}}{\sqrt{1+f_x'^2}}\exp(\mathrm{i}ky\sin\theta_{\rm i}-\mathrm{i}kf\cos\theta_{\rm i}) \\
&\quad\times(-\cos\theta\sin\varphi E^{\rm s}_{\rm v\varphi}+\cos\varphi E^{\rm s}_{\rm v\theta})\,\mathrm{d}S, \qquad (31)
\end{aligned}$$

where $\boldsymbol{E}^{\rm s}_{\rm vec} = E_0(\hat{\theta}E^{\rm s}_{\rm v\theta} + \hat{\varphi}E^{\rm s}_{\rm v\varphi})$ and $\boldsymbol{H}^{\rm s}_{\rm vmc} = H_0(-\hat{\theta}E^{\rm s}_{\rm v\varphi} + \hat{\varphi}E^{\rm s}_{\rm v\theta})$ are the scattered fields from the cone-cylinder irradiated by $\boldsymbol{E}_{\rm ed}$ and $\boldsymbol{H}_{\rm md}$, respectively. Then, from Eqs. (30) and (31), the total coupling scattered $\boldsymbol{E}^{\rm s}_{\rm v,rc_total}$ field for the vv-polarization may be written as

$$\boldsymbol{E}^{\rm s}_{\rm v,rc_total} = \hat{\theta}(E^{\rm s}_{\rm v,rc} - Z_0 H^{\rm s}_{\rm v,rc}). \tag{32}$$

As is well known, the scattered field can be written as the following expression:[1]

$$\boldsymbol{E}^{\rm s} = [\exp(\mathrm{i}kr)/r]\,\overline{\overline{\boldsymbol{S}}}\,\boldsymbol{E}^{\rm i}, \tag{33}$$

where $\overline{\overline{\boldsymbol{S}}}$ is the factor of the scattering matrix. Therefore, combining Eq. (4) with Eq. (33), we can solve the scattering matrix $\boldsymbol{S}_{\rm r}$, and the scattering matrix $\boldsymbol{S}_{\rm c}$ for the isolated cone-cylinder can be obtained from Eq. (15). The coupling scattering matrix $\boldsymbol{S}_{\rm cr}$ can be calculated from Eqs. (27) and (32).

It can be proved that $\overline{\overline{\boldsymbol{S}}}_{\rm rc}$ can be evaluated from $\overline{\overline{\boldsymbol{S}}}_{\rm cr}$ by using the following identity:[1]

$$\overline{\overline{\boldsymbol{S}}}_{\rm rc}(\hat{\boldsymbol{k}}_{\rm s},\hat{\boldsymbol{k}}_{\rm i}) = \overline{\overline{\boldsymbol{S}}}_{\rm cr}^{(-\,{\rm t})}(-\hat{\boldsymbol{k}}_{\rm i},-\hat{\boldsymbol{k}}_{\rm s}), \tag{34}$$

where the superscript $(-t)$ denotes the matrix transposition and multiplication of the off-diagonal elements by –1. Rewriting the above equation in matrix form leads to

$$\begin{aligned}
&\begin{pmatrix} \boldsymbol{S}^{\rm vv}_{\rm rc}(\hat{\boldsymbol{k}}_{\rm i},\hat{\boldsymbol{k}}_{\rm s}) & \boldsymbol{S}^{\rm vh}_{\rm rc}(\hat{\boldsymbol{k}}_{\rm i},\hat{\boldsymbol{k}}_{\rm s}) \\ \boldsymbol{S}^{\rm hv}_{\rm rc}(\hat{\boldsymbol{k}}_{\rm i},\hat{\boldsymbol{k}}_{\rm s}) & \boldsymbol{S}^{\rm hh}_{\rm rc}(\hat{\boldsymbol{k}}_{\rm i},\hat{\boldsymbol{k}}_{\rm s}) \end{pmatrix} \\
&= \begin{pmatrix} \boldsymbol{S}^{\rm vv}_{\rm cr}(-\hat{\boldsymbol{k}}_{\rm s},-\hat{\boldsymbol{k}}_{\rm i}) & -\boldsymbol{S}^{\rm hv}_{\rm cr}(-\hat{\boldsymbol{k}}_{\rm s},-\hat{\boldsymbol{k}}_{\rm i}) \\ -\boldsymbol{S}^{\rm vh}_{\rm cr}(-\hat{\boldsymbol{k}}_{\rm s},-\hat{\boldsymbol{k}}_{\rm i}) & \boldsymbol{S}^{\rm hh}_{\rm cr}(-\hat{\boldsymbol{k}}_{\rm s},-\hat{\boldsymbol{k}}_{\rm i}) \end{pmatrix}. \qquad (35)
\end{aligned}$$

In the case of backscattering, i.e. $\hat{k}_{\rm s} = -\hat{k}_{\rm i}$, equation (35) can be simplified into[1]

$$\begin{pmatrix} \boldsymbol{S}^{\rm vv}_{\rm rc} & 0 \\ 0 & \boldsymbol{S}^{\rm hh}_{\rm rc} \end{pmatrix} = \begin{pmatrix} \boldsymbol{S}^{\rm vv}_{\rm cr} & 0 \\ 0 & \boldsymbol{S}^{\rm hh}_{\rm cr} \end{pmatrix}. \tag{36}$$

The analytical expressions of radar cross section (RCS) for the secondary coupling field and the total composite scattered field can be defined as

$$\sigma_{\rm cr} = 4\pi \ |2\boldsymbol{S}_{\rm cr}|^2 \,, \tag{37}$$

$$\sigma \ = 4\pi \ |\boldsymbol{S}_{\rm r} + 2\boldsymbol{S}_{\rm cr} + \boldsymbol{S}_{\rm c}|^2 \,. \tag{38}$$

The Doppler spectrum is a power spectral density of the random time-varying complex amplitude of the composite scattering field. To evaluate it, we use a standard spectral estimation technique. Thus, the expression of the Doppler spectrum is defined as[15]

$$S(f) = \frac{1}{T}|\int_0^T E^{\rm s}(t,\theta_{\rm i},\theta_{\rm s})\exp(-{\rm i}2\pi ft)\,{\rm d}t|^2, \tag{39}$$

and in the case of backscattering, we have $\theta_{\rm s} = -\theta_{\rm i}$.

5. Numerical results and discussion

In this Section, the numerical simulations and a sensitivity analysis are presented to demonstrate the significance of the scattering interaction between the cone-cylinder target and the dielectric rough sea surface. We first compute the angular distribution of RCS for a cone-cylinder above the sea surface. Figure 7 shows the total backscatterings and coupling RCSs of cone-cylinders with different sizes at a height of $H = 150$ cm above the sea surface ($t = 0$ s) for both hh- and vv-polarizations. In the calculation, the frequency of the incident wave is 10 GHz, the length of the sea surface is 200 m, the windspeed $U_{19.5} = 5$ m/s, and the permittivity of the sea water is (61.0, 33.0). The numerical results are the average of 20 Monte Carlo surface realizations.

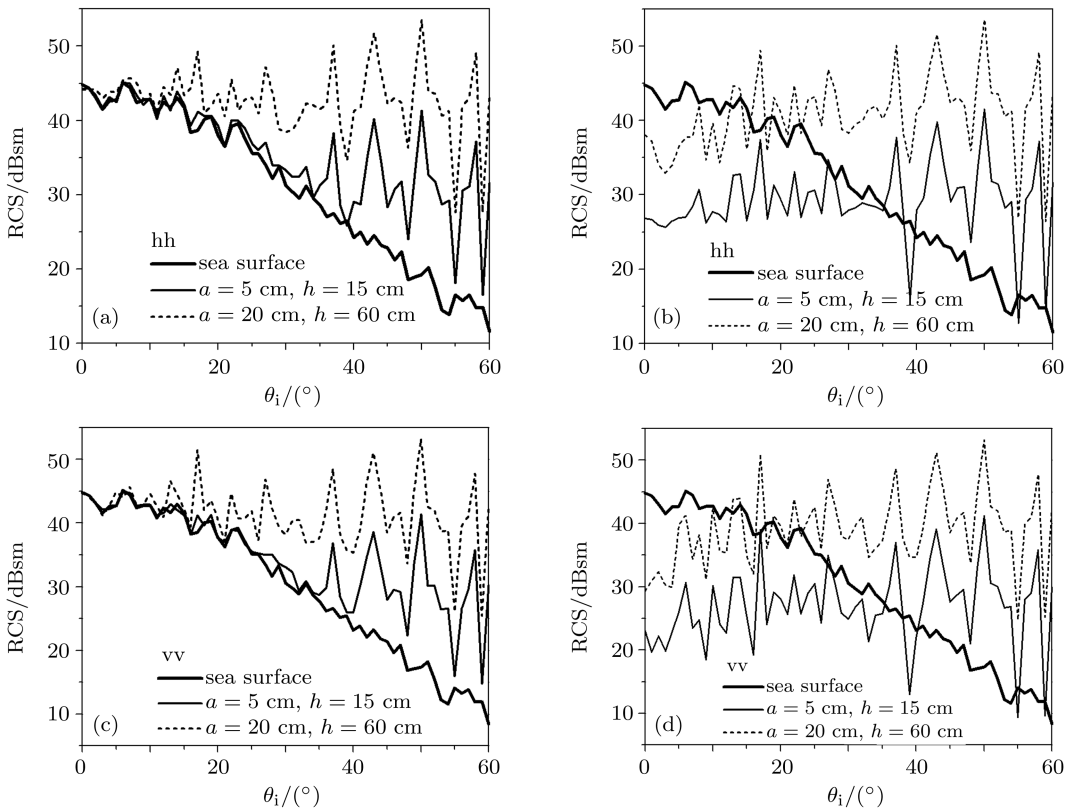


Fig. 7. Angular distributions of backscattering RCS with different sizes of the cone-cylinder. (a): Total backscattering RCS (hh), (b): coupling backscattering RCS (hh), (c): total backscattering RCS (vv), and (d): coupling backscattering RCS (vv).

From Figs. 7(a)–7(d), it is observed that the backscattering RCS of the sea surface only decreases with increasing incident angle, while the total backscattering RCS and the coupling backscattering RCS exhibit more oscillations than those of the surface only (without target), which is due to the fact that the interaction becomes stronger between the target and the surface, in particular for the case of large incident angle. Moreover, when the incident angle is small, the coupling area is so small that the secondary coupling backscattering is not

strong enough and the backscattering from the sea surface plays a leading role in the total scattering field, and it is difficult to distinguish the cone-cylinder from the sea surface. It is also observed that the coupling backscattering RCS increases with the increase of the size of the cone-cylinder, which is visually larger than that only from the sea surface, especially for the cases of large incident angles. This phenomenon is caused mainly by the fact that the interaction between the rough sea surface and the cone-cylinder increases, which leads the secondary coupling backscattering RCS to become large with the size of the cone-cylinder increasing. It should be pointed that only the backscattering pattern for $\theta_{\rm i} < 60°$ is depicted in this paper, which is because the limitation of the conventional KA is invalid for sea surface scattering in the large scattering angle region without considering multiple scattering and the shadowing effect.

In Figs. 8(a) and 8(b), the effects of the total composite backscattering RCS on the wind speeds are plotted for hh-polarization, and vv-polarization, respectively. The relevant parameters are the same as those given in Fig. 7. As shown in Fig. 8, all the total composite backscatterings with different wind speeds are larger than those of the scattering from the sea surface only for both hh-polarization and vv-polarization. The backscattering RCS of the sea surface increases with the increase of the winds peed, which is due to the increase of the roughness of the sea surface. As far as the total composite backscattering is concerned, it is found that as the wind speed increases, the composite backscattering almost does not change. The above result indicates that the effect of the wind speed on the tendency of the secondary coupling backscattering cross section is very small, in other words, the coupling scattering is not "sensitive" to the variation of the wind speed. This result is just similar to that of the sphere-rough surface composite model given in our previous work.[26]

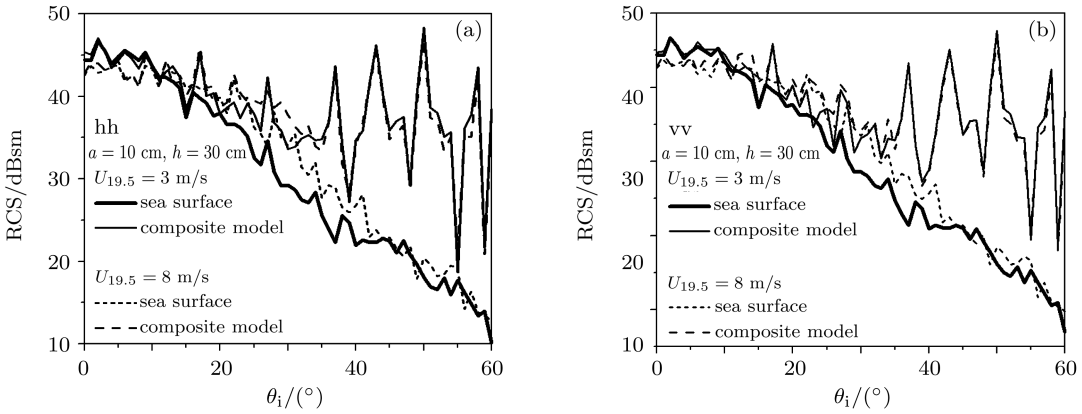


Fig. 8. Backscattering RCSs for different wind speeds, (a): hh-polarization, and (b): vv-polarization.

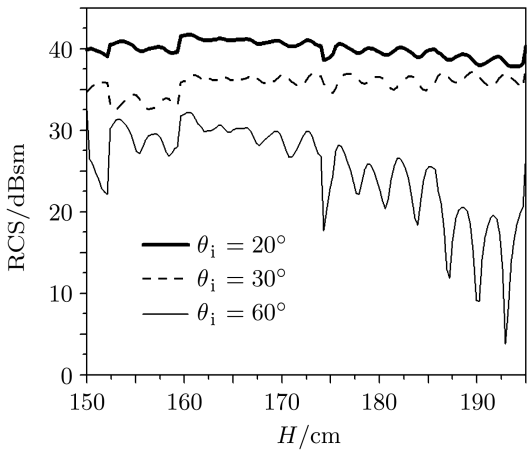


Fig. 9. Dependence of the backscattering RCS on the height of the cone-cylinder above the sea surface.

The dependences of the variation in total backscattering RCS (hh-polarization) with height H between the cone-cylinder target and the rough surface are also presented in Fig. 9 for different incident angles, where the size of the cone-cylinder is given by $a = 10$ cm, $h = 30$ cm, the other parameters are the same as those in Fig. 7. As clearly shown in Fig. 9, the total backscattering RCS has an oscillation instead of a monotonic change with the increase of the height. In the case of the small incident angles ($\theta_{\rm i} = 20°,\ \ 30°$), the backscattering field of the sea surface plays a leading role, the coupling scattering is small as mentioned in Fig. 7, hence, the total backscattering RCS changes very little with the variation of H. However,

for the large incident angle ($\theta_{\rm i} = 60°$), the contribution of the coupling scattering component becomes strong in the total scattering, which results in a more oscillating behaviour of scattering for the composite model. In addition, it is also found that the tendency of the composite scattering decreases with the increase of H, especially for the large incident angle, which we also attribute to the fact that the actual coupling scattering becomes small with the value of H increasing.

For the figures of Doppler spectrum which follow, most of the relevant parameters in the calculation are displayed correspondingly. In Figs. 10–13, the permittivity of the sea water is (61.0, 33.0) and the frequency of the incident wave 10 GHz. The size and the height of the cone-cylinder are $a = 10$ cm, $h = 30$ cm and $H = 150$ cm, respectively.

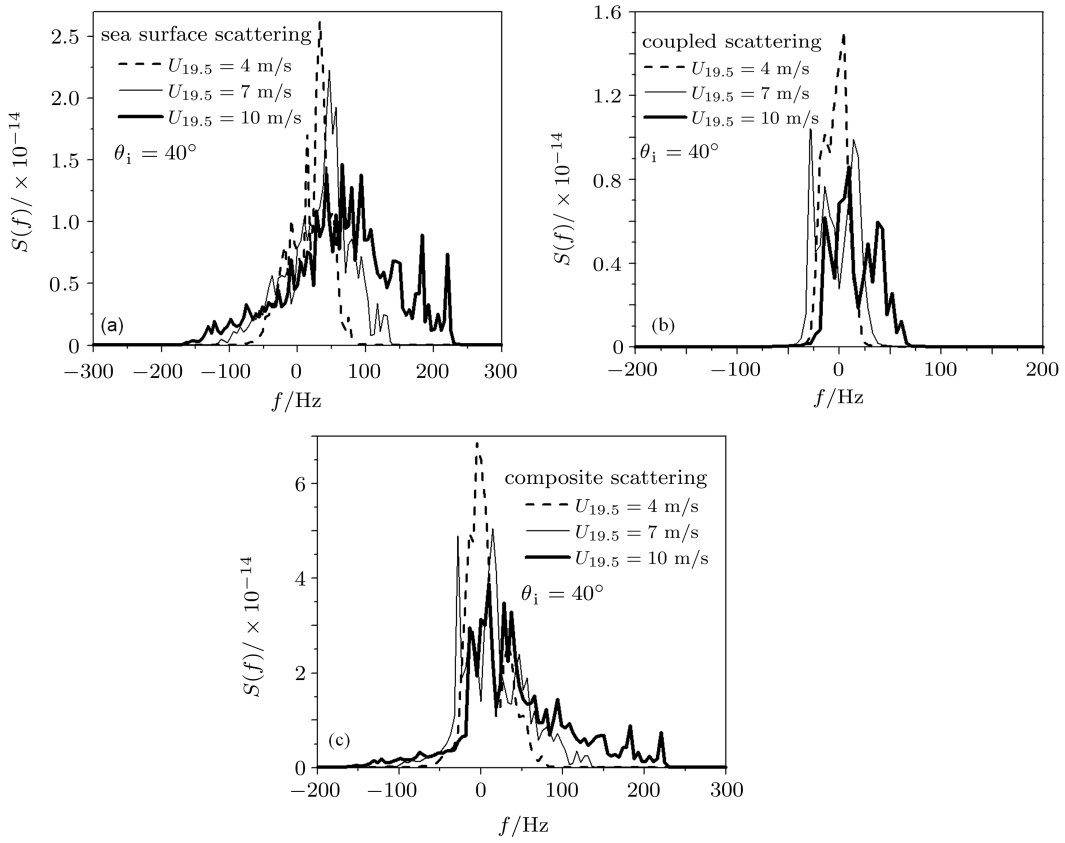


Fig. 10. Doppler spectra of the backscattered field for different wind speeds, (a): only surface scattering, (b): coupled scattering, and (c): composite scattering.

Figures 10(a)–10(c) show the Doppler spectra of the backscattered field from the sea surface only and the total composite backscattered field with different wind speeds for hh-polarization. From Fig. 10(a), we can find that as wind speed increases, the velocities of the surface water and the orbital motion of the sea wave increase on a large-scale, and for the Doppler spectrum of the backscattering from the oceanic surface, there appears to be a gradual increase in Doppler spectrum frequency shift, which is coincident with the measurement results given by Rozenberg *et al.*[27] On the other hand, there also exists a broadening for the lobe of the Doppler spectra with increasing wind speed. The above phenomenon should not be really surprising; the primary reason for this is that the incoherent scattering increases with an increase in the roughness of the oceanic surface, and thus the backscattering energy will be distributed over a wide region of the frequency domain, which has been discussed in Refs. [28]–[30]. Similar to the case in Fig. 10(a), the Doppler spectra of the coupled and the composite backscattering fields become broader with the increase of the wind speed (see Figs. 10(b) and 10(c), respectively), which is similar to the case in Fig. 10(a), however, their frequency shifts have almost no increase, which is unlike the scenario in Fig. 10(a). The main reason may be ascribed to the existence of the deterministic target (cone-cylinder), which leads the "roughness" of the composite model to decrease, thereby causing the incoherent scattering to decrease. Moreover, all the maximum values of spectral density of the Doppler spectrum for the composite model and the surface only become small with the increase of wind speed.

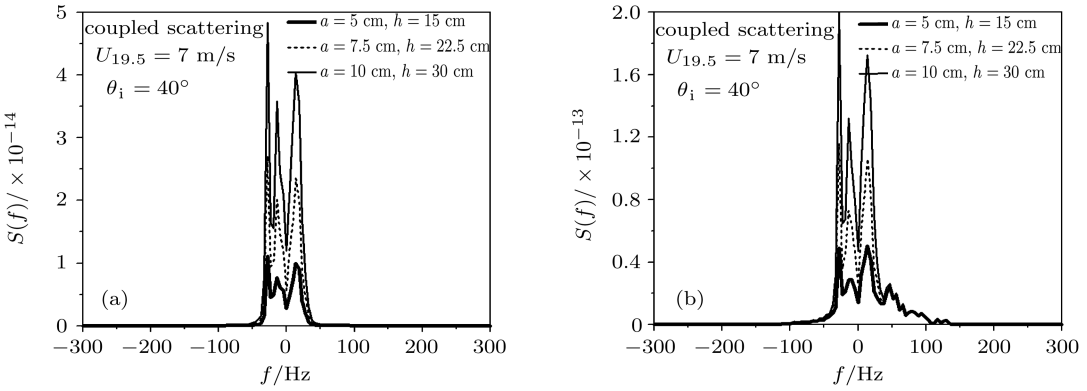


Fig. 11. Doppler spectra of the backscattered field for different sizes of the cone-cylinder, (a): coupled scattering, and (b): composite scattering.

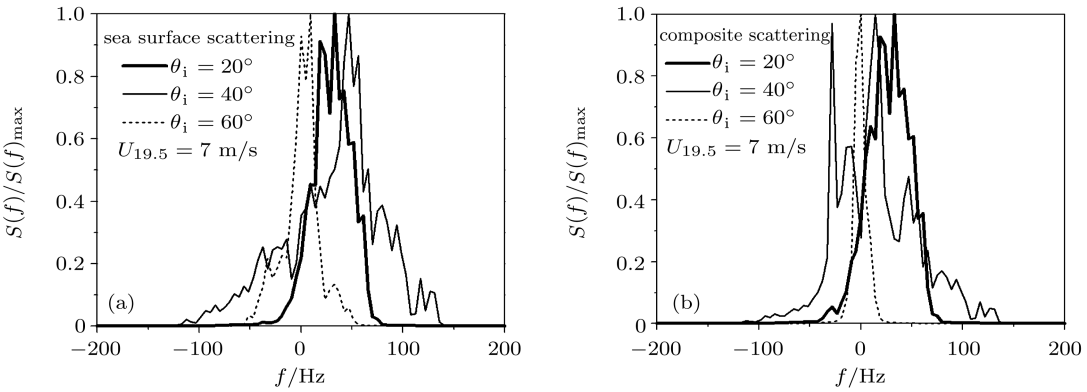


Fig. 12. Comparison of the Doppler spectral width between the sea surface and the composite models with different incident angles, (a): sea surface backscattering, and (b): composite backscattering.

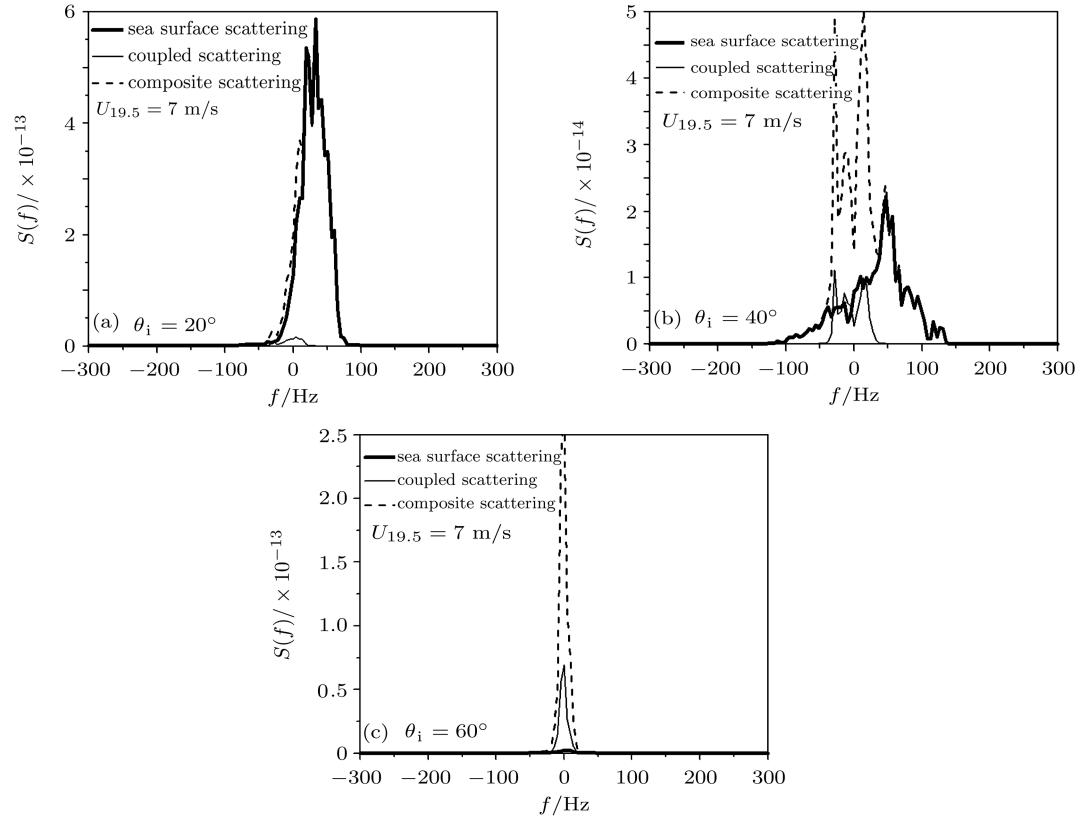


Fig. 13. Doppler spectra of the backscattered field for different incident angles: (a) $\theta_i = 20°$, (b) $\theta_i = 40°$, (c) $\theta_i = 60°$.

The changes in Doppler spectra of the composite and the coupled backscattered field with cone-cylinder size for hh-polarization are presented in Fig. 11. It shows that the amplitudes of the spectra become larger with increasing cone-cylinder size, as well as the previous composite backscattering cross section in Fig. 7. It should be noted that this may be due to the fact that the composite and the coupled backscattering cross sections become stronger as the cone-cylinder size increases.

To further explore the Doppler characteristic of the target-rough surface model, in Fig. 12, we consider the effect of incident angle on the normalized Doppler spectrum of the sea and the composite backscattered fields for hh-polarization. An interesting feature that is worth noting is the behaviour of the spectral width. As seen in Fig. 12, with increasing incident angle, both the Doppler spectra for the sea surface and the composite models first broaden (as shown for $\theta_{\rm i} = 40^\circ$), then shrink (as shown for $\theta_{\rm i} = 60^\circ$), which is consistent with the results given by Toporkov *et al.*[15] In order to properly describe and analyse the phenomenon shown in Fig. 12, the Doppler spectra of the backscattered field, including the sea surface scattering, the coupled scattering, as well as the composite scattering, with different incident angles are presented in Figs. 13(a)–13(c) for hh-polarization. It can be readily seen that with a small incident angle, the amplitude of the Doppler spectrum of the coupled backscattered field is much smaller than that of the sea surface only and that of the composite model, and in this case, the Doppler spectra of backscattering from the cone-cylinder target and the coupling scattering from the composite model are entirely covered by the spectrum of the sea clutter. Therefore, hardly any information about the target from the Doppler spectrum of the composite model is obtained. As the incident angle increases up to $\theta_{\rm i} = 40^\circ$, the amplitude of the Doppler spectrum of the composite model becomes larger than that of the sea surface only, and the Doppler spectrum shift of the rough sea surface only is apparently separated from that of the composite model. Meanwhile, the amplitude of the Doppler spectrum of the coupled field gradually becomes large, however, it is still smaller than that of the sea surface only. When the incident angle $\theta_{\rm i} = 60^\circ$, the amplitude of the Doppler spectrum of the sea surface is very small, consequently, the influence of the Doppler spectrum of the coupling backscattering on the total Doppler spectrum of the composite model becomes important, and the Doppler spectrum of the coupling backscattering will emerge in the Doppler spectrum of the backscattering from the sea surface. In this case, the existence of the target is easily known due to the fact that the Doppler spectrum of the coupling backscattering is easily distinguished from the spectrum of the sea clutter, which is of great importance for target detection above the oceanic surface, especially for the larger incident angle. Similar conclusions about the Doppler spectrum can also be obtained for vv-polarization.

6. Conclusions

This paper presents a study of electromagnetic scattering from a cone-cylinder above a time-varying dielectric sea surface by using the MEC theory and reciprocity theorem. Compared with the traditional numerical simulations, the edge diffraction of the target is taken into account in the composite scattering, and this method overcomes the problem of the vast memory and computational requirements for the electrical large-size targets, which results in the problem of electromagnetic scattering from the target above the surface becoming easier to solve. Using a combination of RT with the MEC and KA methods, the dependences of the backscattering RCS and the Doppler spectrum of the backscattering field on the size of the target, the wind speed, and the incident angle are numerically demonstrated and discussed. What is worth noting is that the Doppler spectrum of the coupling backscattering and that of the cone-cylinder target are covered by the Doppler spectrum of the sea clutter with small incident angle, thus, it is difficult to obtain information about the target from the Doppler spectrum of the composite model. With increasing incident angle, the contribution of the coupling scattering field to the total scattering increases gradually, the Doppler spectrum of the coupling backscattering becomes more prominent and important, which is of great significance for target detection with large angle incidence.

This paper only deals with the problem of composite scattering from a target above a one-dimensional time-varying dielectric sea surface, so further investigation should include composite scattering from an actually moving target above a sea surface with low grazing angle incidence under the modified KA. For composite

scattering from a target above a two-dimensional dielectric sea surface, our numerical simulations also need to be verified by some absolutely exact numerical method and by experiment in future work.

References

[1] Chiu T and Sarabandi K 1999 *IEEE Trans. Antennas. Propag.* **47** 902

[2] Jamil K and Burkholder R J 2006 *IEEE Trans. Geosci. Remote Sensing.* **44** 3330

[3] Holliday D, DeRaad L L and St-Cyr G J 1996 *IEEE Trans. Antennas. Propag.* **44** 722

[4] Liu P and Jin Y Q 2005 *IEEE Trans. Antennas. Propag.* **53** 825

[5] Li J, Guo L X and Zeng H 2008 *Waves in Random and Complex Media* **18** 641

[6] Wang R and Guo L X 2009 *J. Opt. Soc. Am.* A **26** 517

[7] Guo L X, Wang A Q and Ma J 2009 *Progress in Electromagnetic Research* **89** 149

[8] Ye H X and Jin Y Q 2006 *IEEE Trans. Geosci. Remote Sensing.* **44** 108

[9] Rodriguez P M, Landesa L, Rodriguez J L, Obelleiro F and Burkholder R J 1999 *IEEE Trans. Antennas. Propag.* **47** 961

[10] Kubicke G, Bourlier C and Saillard J 2008 *Waves in Random and Complex Media* **18** 495

[11] Li J, Guo L X and Zeng H 2008 *Progress in Electromagnetics Research* **88** 197

[12] Li J and Guo L X 2009 *Chin. Phys.* B **18** 2757

[13] Li L, He J Q, Liu Z J and Carin L 2003 *IEEE Trans. Antennas. Propag.* **51** 810

[14] Guo L X and Kim C Y 2002 *Microw. Opt. Technol. Lett.* **33** 142

[15] Toporkov J V and Brown G S 2000 *IEEE Trans. Geosci. Remote Sensing.* **38** 1616

[16] Chen J, Lo K Y, Leung H and Litva J 1996 *IEEE Trans. Geosci. Remote Sensing.* **34** 966

[17] Wang M G 1994 *Theory of Geometry Diffraction* (Xi'an: Xidian University Press)

[18] Michaeli A 1984 *IEEE Trans. Antennas. Propag.* **32** 252

[19] Michaeli A 1986 *IEEE Trans. Antennas. Propag.* **34** 912

[20] Ando M 1991 *IEEE Proceedings-H.* **138** 289

[21] Michaeli A 1986 *IEEE Trans. Antennas. Propag.* **34** 1034

[22] Tiberio R and Maci S 1995 *IEEE Trans. Antennas. Propaga.* **43** 87

[23] Johansen P M and Breinberg O 1995 *IEEE Trans. Antennas. Propag.* **43** 689

[24] Cui S M, Wu Z S and Fang D G 1997 *Journal of Microwaves* **3** 20

[25] Ivrissimtzis L P and Marhefka R J 1992 *IEEE Trans. Antennas. Propag.* **40** 1302

[26] Guo L X, Wang Y H and Wu Z S 2008 *Sci. Chin.* Ser. G: *Phys. Mech. Astron.* **51** 269

[27] Rozenberg A D, Quigley D C and Melville W K 1995 *IEEE Trans. Geosci. Remote Sensing.* **33** 1037

[28] Johnson J T, Toporkov J V and Brown G S 2001 *IEEE Trans. Geosci. Remote Sensing.* **39** 2411

[29] Toporkov J V and Brown G S 2002 *IEEE Trans. Antennas. Propaga.* **50** 417

[30] Guo L X, Wang Y H and Wu Z S 2005 *Acta Phys. Sin.* **54** 96 (in Chinese)